

1 STANDARD MODEL IS BEST MODEL (WORKING TITLE)

2 William Kennedy DiClemente

3 A DISSERTATION

4 in

5 Physics and Astronomy

6 Presented to the Faculties of The University of Pennsylvania

7 in Partial Fulfillment of the Requirements for the Degree of Doctor of Philosophy

8 2018 Last compiled: December 28, 2018

9

10 I. Joseph Kroll, Professor, Physics

11 Supervisor of Dissertation

12

13 Joshua Klein, Professor, Physics

14 Graduate Group Chairperson

15 Dissertation Committee

16 (Committee Prof. 1), Professor, Physics

17 (Committee Prof. 2), Associate Professor, Physics

18 (Committee Prof. 3), Professor, Physics

19 (Committee Prof. 4), Professor, Physics

20 I. Joseph Kroll, Professor, Physics

21

STANDARD MODEL IS BEST MODEL (WORKING TITLE)

22

COPYRIGHT

23

2018

24

William Kennedy DiClemente

25

All rights reserved.

Acknowledgements

27 I'd like to thanks the Ghosts of Penn Students Past for providing me with such an amazing thesis
28 template.

29

ABSTRACT

30

STANDARD MODEL IS BEST MODEL (WORKING TITLE)

31

William Kennedy DiClemente

32

J. Kroll

33

This is the abstract text.

Contents

35	Acknowledgements	iii
36	Abstract	iv
37	Contents	v
38	List of Tables	viii
39	List of Figures	ix
40	Preface	x
41	1 Introduction	1
42	2 Theoretical Framework	2
43	2.1 Introduction to the Standard Model	2
44	2.2 Electroweak Mixing and the Higgs Field	2
45	3 LHC and the ATLAS Detector	3
46	3.1 The Large Hadron Collider	3
47	3.2 The ATLAS Detector	3
48	3.2.1 The Inner Detector	3
49	3.2.1.1 Pixel Detector	3
50	3.2.1.2 Semiconductor Tracker	3
51	3.2.1.3 Transition Radiation Tracker	3
52	3.2.2 The Calorimeters	4

53	3.2.2.1	Liquid Argon Calorimeters	4
54	3.2.2.2	Tile Calorimeters	4
55	4	Alignment of the ATLAS Inner Detector	5
56	4.1	Effects of Misalignment	5
57	4.2	The Alignment Method	5
58	4.3	Momentum Bias Corrections	5
59	4.4	Alignment of the IBL	6
60	4.5	Alignment Monitoring	6
61	5	WZ production @ $\sqrt{s} = 13$ TeV	7
62	5.1	Theoretical motivation	7
63	5.2	Signal definition	7
64	5.3	Background estimations	7
65	5.4	Cross section measurement	7
66	6	Same-sign WW @ $\sqrt{s} = 13$ TeV	8
67	6.1	Theoretical motivation	8
68	6.2	Signal definition	8
69	6.3	Background estimations	8
70	6.4	Cross section measurement	8
71	7	Prospects for same-sign WW at the High Luminosity LHC	9
72	7.1	Theoretical motivation	9
73	7.2	Monte Carlo samples	10
74	7.3	Signal definition	11
75	7.3.1	Sensitivity to longitudinal polarization	11
76	7.4	Background estimations	11
77	7.4.1	Truth based isolation	11
78	7.5	Event selection	11
79	7.6	Selection optimization	13
80	7.6.1	Random grid search algorithm	13
81	7.6.2	Inputs to the optimization	15
82	7.6.3	Results of the optimization	16

83	7.7 Results	18
84	7.7.1 Event yields	18
85	7.7.2 Uncertainties	18
86	7.7.3 Cross section measurement	18
87	8 Conclusion	21
88	Bibliography	22

List of Tables

90	7.1	derp	11
91	7.2	Updates to the $W^\pm W^\pm jj$ event selection criteria after optimization. Cuts not listed	
92		remain unchanged from the default selection in Table 7.1.	17

List of Figures

94	3.1	General cut-away view of the ATLAS detector.	4
95	7.1	Comparison of the leading (top) and subleading (bottom) lepton p_T distributions for 96 purely longitudinal (LL, black) and mixed polarization (LT+TT, cyan) $W^\pm W^\pm jj$ events. 97 Plots from [1].	12
98	7.2	Comparison of the azimuthal dijet separation ($ \Delta\phi_{jj} $) for purely longitudinal (LL, black) 99 and mixed polarization (LT+TT, cyan) $W^\pm W^\pm jj$ events. Plot from [1].	13
100	7.3	A visual representation of a rectangular grid search algorithm. The signal events are the 101 blue triangles, and the red circles are the background events. TODO: replace with own 102 figure	14
103	7.4	A visual representation of a random grid search algorithm. The signal events are the 104 blue triangles, and the red circles are the background events. TODO: replace with own 105 figure	15
106	7.5	Leading lepton p_T distribution. The default and optimized cuts are represented by the 107 red and green dashed lines, respectively. The $W^\pm W^\pm jj$ EWK signal (black points) is 108 normalized to the same area as the sum of the backgrounds (colored histogram). TODO: 109 Move to appendix or omit	17
110	7.6	Dilepton invariant mass distribution. The default and optimized cuts are represented by 111 the red and green dashed lines, respectively. The $W^\pm W^\pm jj$ EWK signal (black points) is 112 normalized to the same area as the sum of the backgrounds (colored histogram). TODO: 113 Move to appendix or omit	18
114	7.7	Leading (top) and subleading (bottom) jet p_T distributions. The default and optimized 115 cuts are represented by the red and green dashed lines, respectively. The $W^\pm W^\pm jj$ EWK 116 signal (black points) is normalized to the same area as the sum of the backgrounds 117 (colored histogram).	19
118	7.8	Dijet invariant mass distribution. The default and optimized cuts are represented by the 119 red and green dashed lines, respectively. The $W^\pm W^\pm jj$ EWK signal (black points) is 120 normalized to the same area as the sum of the backgrounds (colored histogram). TODO: 121 Move to appendix or omit	20
122	7.9	Lepton-jet centrality distribution. The default and optimized cuts are represented by the 123 red and green dashed lines, respectively. The $W^\pm W^\pm jj$ EWK signal (black points) is 124 normalized to the same area as the sum of the backgrounds (colored histogram).	20

Preface

126 This is the preface. It's optional, but it's nice to give some context for the reader and stuff.

Will K. DiClemente
Philadelphia, February 2019

128

CHAPTER 1

129

Introduction

130 The Standard Model (SM)¹ has been remarkably successful...

¹Here's a footnote.

CHAPTER 2

Theoretical Framework

(Some example introductory text for this chapter)...

2.1 Introduction to the Standard Model

Modern particle physics is generally interpreted in terms of the Standard Model (SM). This is a quantum field theory which encapsulates our understanding of the electromagnetic, weak, and strong interactions...

2.2 Electroweak Mixing and the Higgs Field

When the theory of the electroweak interaction was first developed [2, 3], the W and Z bosons were predicted to be massless (a typical mass term in the Lagrangian would violate the $SU(2)$ symmetry). However, these were experimentally observed to have masses...

CHAPTER 3

LHC and the ATLAS Detector

3.1 The Large Hadron Collider

The Large Hadron Collider (LHC) [4] is...

3.2 The ATLAS Detector

ATLAS is a general-purpose particle detector...

3.2.1 The Inner Detector

The Inner Detector serves the primary purpose of measuring the trajectories of charged particles...

3.2.1.1 Pixel Detector

The Pixel detector consists of four cylindrical barrel layers and three disk-shaped endcap layers...

3.2.1.2 Semiconductor Tracker

The Semiconductor Tracker uses the same basic technology as the Pixels, but the fundamental unit of silicon is a larger “strip”...

3.2.1.3 Transition Radiation Tracker

The Transition Radiation Tracker is the outermost component of the ID...

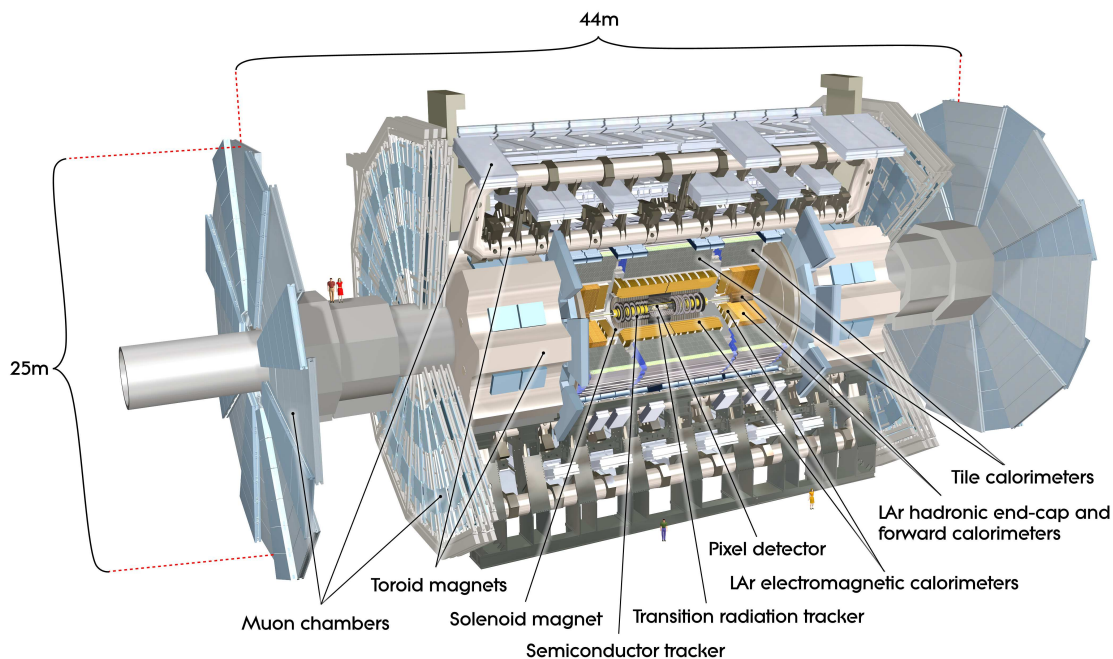


Figure 3.1: General cut-away view of the ATLAS detector [5].

3.2.2 The Calorimeters

ATLAS includes two types of calorimeter system for measuring electromagnetic and hadronic showers. These are the Liquid Argon (LAr) calorimeters and the Tile calorimeters. Together, these cover the region with $|\eta| < 4.9$...

3.2.2.1 Liquid Argon Calorimeters

The Liquid Argon system consists of...

3.2.2.2 Tile Calorimeters

The Tile calorimeter provides coverage for hadronic showers...

165

CHAPTER 4

166

Alignment of the ATLAS Inner Detector

167 In order for the subdetectors of the ID to operate at their designed precisions, it is essential that
168 the locations of the sensors be known as precisely as possible. Differences between the expected and
169 actual positions of a sensor can result in displaced particle hits and degrade track reconstruction
170 quality. These misalignments can occur for any number of reasons, including but not limited to
171 elements shifting during maintenance periods or cycles in ATLAS's magnetic field, or simply small
172 movements during normal detector operations. Since it is not practical to physically realign hundreds
173 of thousands of detector elements to μm precision by hand, an iterative track-based alignment
174 algorithm is used to determine the physical positions and orientations of these elements [6]. The
175 effects of misalignments and the steps taken to correct and monitor them are detailed in this chapter.

176 4.1 Effects of Misalignment

177 Hello world!

178 4.2 The Alignment Method

179 Hello world!

180 4.3 Momentum Bias Corrections

181 Hello world!

182 **4.4 Alignment of the IBL**

183 Hello world!

184 **4.5 Alignment Monitoring**

185 Hello world!

186

CHAPTER 5

187

WZ production @ $\sqrt{s} = 13$ TeV

188 **5.1 Theoretical motivation**

189 Hello world!

190 **5.2 Signal definition**

191 Hello world!

192 **5.3 Background estimations**

193 Hello world!

194 **5.4 Cross section measurement**

195 Hello world!

196

CHAPTER 6

197

Same-sign WW @ $\sqrt{s} = 13$ TeV

198 6.1 Theoretical motivation

199 Hello world!

200 6.2 Signal definition

201 Hello world!

202 6.3 Background estimations

203 Hello world!

204 6.4 Cross section measurement

205 Hello world!

CHAPTER 7

Prospects for same-sign WW at the High Luminosity LHC

On December 3, 2018, Run 2 of the LHC officially ended, and the collider was shut down to begin the first of two scheduled extended maintenance periods [7]. During these two long shutdowns, the Phase-I and Phase-II upgrades of the LHC and ATLAS will occur in order to prepare for the High-Luminosity LHC (HL-LHC) which is scheduled to begin operation in 2026 [8].

The HL-LHC is planned to run at an instantaneous luminosity of $\mathcal{L} = 5 \times 10^{34} \text{ cm}^{-2}\text{s}^{-1}$ with an average of 140 collisions per beam-crossing. Over the course of operation, the HL-LHC is expected to collect a total integrated luminosity of $\mathcal{L} = 3000 \text{ fb}^{-1}$ by 2035 [9].

These run conditions are much harsher than what ATLAS has experienced so far, and as a result there are several planned upgrades to the detector. Most notably, the entire ID will be replaced with an all-silicon tracker which will extend the coverage from $|\eta| \leq 2.7$ up to $|\eta| \leq 4.0$. This will allow for reconstruction of charged particle tracks which can in turn be matched to clusters in the calorimeters for electron identification or forward jet tagging [10].

TODO: Why are we studying ssww at the HL-LHC

7.1 Theoretical motivation

The theoretical motivation for studying the ssWW process is detailed in Section 6.1.

7.2 Monte Carlo samples

As no real HL-LHC data will be available for many years, all processes in this prospects study must be simulated using Monte Carlo (MC) generators. Signal and background processes were generated at $\sqrt{s} = 14$ TeV, and the event yields scaled to the anticipated HL-LHC integrated luminosity of $\mathcal{L} = 3000 \text{ fb}^{-1}$.

TODO: Consider putting all this in a table

The signal sample consists of both VBS and non-VBS electroweak (EWK) $W^\pm W^\pm jj$ production, and it is simulated with the `Madgraph5_aMC@NLO` generator [11] using the `NNPDF3.0` PDF set [12] and interfaced with `PYTHIA v8` [13] for hadronization and parton showering. To study the longitudinal polarization more directly, two additional `Madgraph5_aMC@NLO` $W^\pm W^\pm jj$ samples are used: one containing only the longitudinal contribution (LL) and a second containing the transverse (TT) and mixed (LT) contributions.

TODO: Here we talk about things that mimic the experimental signature before we formally state what the signal is... There are many other processes that can produce the same final state as the $W^\pm W^\pm jj$ and must also be accounted for using MC simulations. WZ events are generated using `SHERPA v2.2.0` [14, 15, 16], which includes up to one parton at next-to-leading order (NLO) in the strong coupling constant α_s and up to three additional partons at leading order (LO). Both EWK and QCD production are included in these samples. ZZ events are generated using `SHERPA v2.2.2` with up to two additional partons in the final state. Triboson backgrounds $VVV, V = W, Z$ where the bosons can decay leptonically or hadronically are simulated with `SHERPA v2.2.2` with up to two additional partons in the final state. W +jets backgrounds are generated for electron, muon, and tau final states are generated at LO with `Madgraph5_aMC@NLO` and the `NNPDF3.0` set with showering from `PYTHIA v8`. Z +jets events are generated using `POWHEG-BOX` [17] and the `CT10` PDF set [18] interfaced with `PYTHIA v8`. Finally, $t\bar{t}$ and single-top events are generated using `POWHEG-BOX` with showering from `PYTHIA v6`.

Since the MC samples used in the analysis are generated at particle-level and have not been run through the typical full simulation of the ATLAS detector, smearing functions are instead used to estimate detector effects. These are derived from a `GEANT4` simulation of the detector [19].

7.3 Signal definition

The experimental signature of interest here is identical to the 13 TeV analysis detailed in Chapter 6: two prompt leptons (electrons or muons) with the same charge, missing transverse energy, and two jets. Once again the two leading jets are required to have a large angular separation and a high combined invariant mass to enhance the EWK VBS production.

7.3.1 Sensitivity to longitudinal polarization

7.4 Background estimations

TODO: MC samples, what we estimate directly from MC, Charge flip, fakes, and isolation

7.4.1 Truth based isolation

7.5 Event selection

TODO: Add table for full lepton (pre-)selection, full jet (pre-)selection, and then finally the overall event selection

Selection requirement	Selection value
Lepton kinematics	$p_T > 25$ GeV $ \eta \leq 4.0$
Jet kinematics	$p_T > 30$ GeV for $ \eta \leq 4.5$ $p_T > 70$ GeV for $ \eta > 3.8$
Dilepton charge	Exactly two signal leptons with same charge
Dilepton separation	$\Delta R_{l,l} \geq 0.3$
Dilepton mass	$m_{ll} > 20$ GeV
Z boson veto	$ m_{ee} - m_Z > 10$ GeV (ee -channel only)
E_T^{miss}	$E_T^{\text{miss}} > 40$ GeV
Jet selection	At least two jets with $\Delta R_{l,j} > 0.3$
b jet veto	$N_{b\text{-jet}} = 0$
Dijet separation	$\Delta \eta_{jj} > 2.5$
Trilepton veto	No additional preselected leptons
Dijet mass	$m_{jj} > 500$ GeV
Lepton-jet centrality ²	$\zeta > 0$

Table 7.1: derp

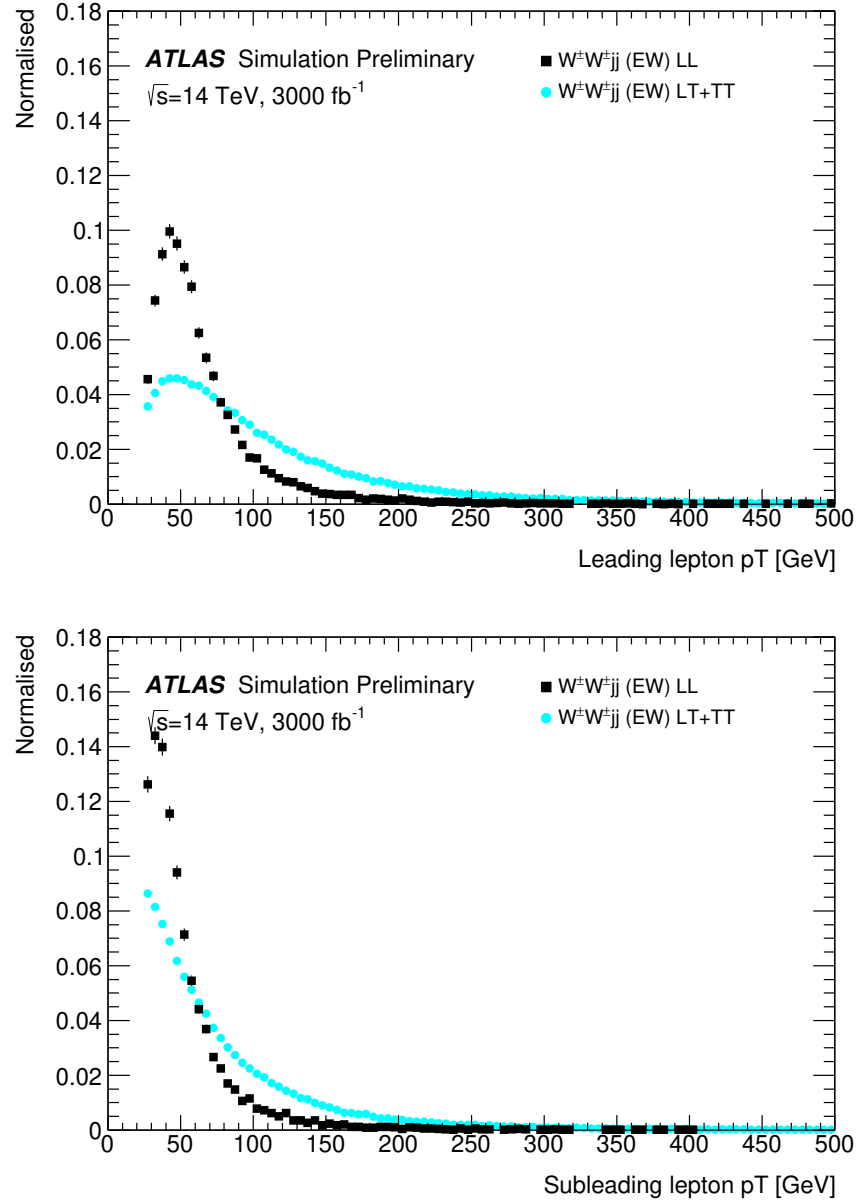


Figure 7.1: Comparison of the leading (top) and subleading (bottom) lepton p_T distributions for purely longitudinal (LL, black) and mixed polarization (LT+TT, cyan) $W^\pm W^\pm jj$ events. Plots from [1].

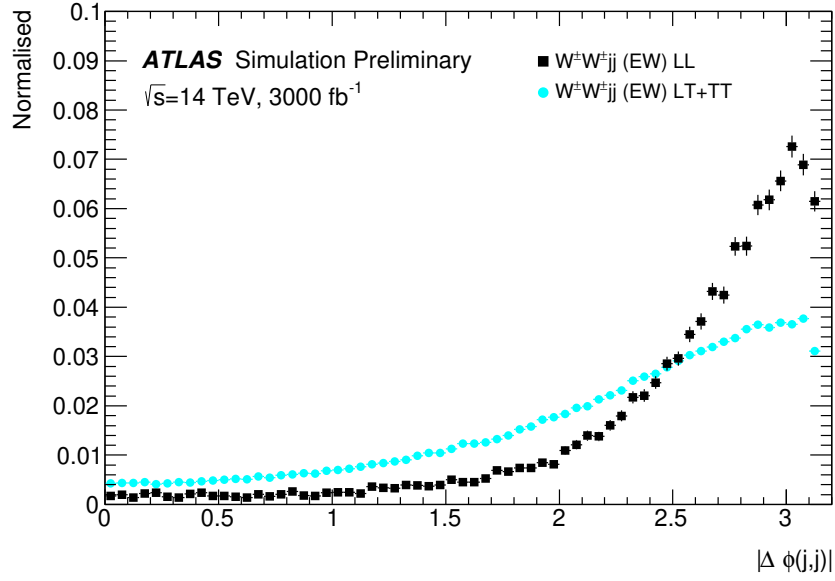


Figure 7.2: Comparison of the azimuthal dijet separation ($|\Delta\phi_{jj}|$) for purely longitudinal (LL, black) and mixed polarization (LT+TT, cyan) $W^\pm W^\pm jj$ events. Plot from [1].

264 7.6 Selection optimization

265 As mentioned earlier, the HL-LHC will feature forward tracking, an increase in center of mass energy,
 266 and a higher integrated luminosity. Therefore, this study is an excellent time to see if there are new
 267 optimizations to the signal event selection that can improve the signal to background ratio.

268 7.6.1 Random grid search algorithm

269 The chosen method for optimizing the event selection is a cut-based algorithm known as the Random
 270 Grid Search (RGS) [20]. Consider a simple case of two variables x and y chosen to differentiate the
 271 signal from the background. In order to be considered a signal event, a given event would be required
 272 to pass a *cut point* $c = \{x > x_c, y > y_c\}$. A simple method to choose the optimal cut point (i.e. the
 273 “best” values of the cuts x_c and y_c) would be to construct an $n \times m$ rectangular grid in x and y
 274 consisting of points $(x_0, y_0), (x_1, y_1), \dots, (x_n, y_m)$, as in Figure 7.3. One can then choose a cut point
 275 $c_k = \{x > x_i, y > y_j\}$ that maximizes the signal significance as measured by a chosen metric. This
 276 would be considered a *regular* or *rectangular* grid search.

277 While effective in principle, this rectangular grid search comes with two major drawbacks:

1. The algorithm does not scale well as the number of variables to be optimized—the dimensionality of the grid—increases. In the case of a square grid with N bins per variable v , the number of cut points to be evaluated grows as N^v .
2. Signal and background samples are rarely evenly distributed over the entire grid, resulting in many cut points being sub-optimal and evaluating them would be a waste of computing resources.

To combat these limitations, the RGS algorithm constructs a grid of cut points directly from the signal sample itself. In the two-dimensional example, this means that the variables x_i and y_j making up the cut point $c_k = \{x > x_i, y > y_j\}$ take their values directly from a given signal event. This has the benefit of creating a *random grid* of cut points that is by construction biased towards regions of high signal concentration. This reduces the need for exponentially increasing numbers of cut points while ensuring that computing resources are not wasted in regions with few to no signal events. An example of the the two-dimensional random grid is shown in Figure 7.4.

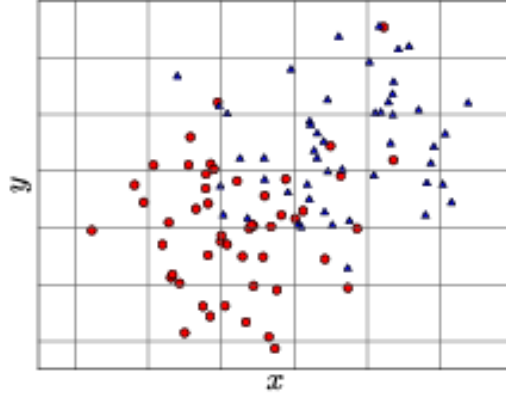


Figure 7.3: A visual representation of a rectangular grid search algorithm. The signal events are the blue triangles, and the red circles are the background events. **TODO: replace with own figure**

Once the random grid of cut points is constructed, the optimal cut point can be chosen using whatever metric the analyzer chooses, such as signal to background ratio. For the purpose of the $W^\pm W^\pm jj$ upgrade study, the optimal cut point is the one that mazimizes the signal significance Z defined as in Equation 7.1 [21].

$$Z = \sqrt{2 \left[(s+b) \ln \left(\frac{s+b}{b_0} \right) + b_0 - s - b \right] + \frac{(b-b_0)^2}{\sigma_b^2}} \quad (7.1)$$

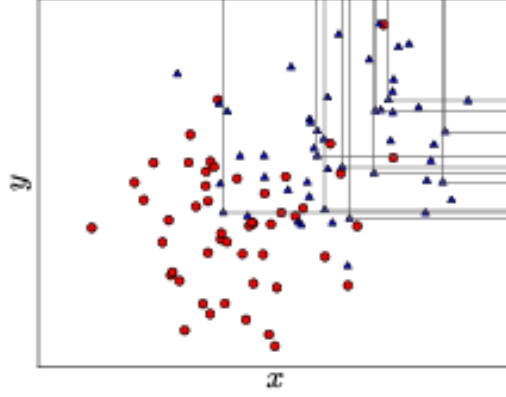


Figure 7.4: A visual representation of a random grid search algorithm. The signal events are the blue triangles, and the red circles are the background events. **TODO: replace with own figure**

where s and b are the number of signal and background events, respectively, σ_b is the total uncertainty on the background, and b_0 is defined as:

$$b_0 = \frac{1}{2} \left(b - \sigma_b^2 + \sqrt{(b - \sigma_b^2)^2 + 4(s + b)\sigma_b^2} \right) \quad (7.2)$$

In the case where the background is known precisely (i.e. $\sigma_b = 0$), Equation 7.1 simplifies to

$$Z = \sqrt{2 \left(b \left[(1 + s/b) \ln(1 + s/b) - s/b \right] \right)} \quad (7.3)$$

which further reduces to the familiar $Z = s/\sqrt{b}$ for the case when $s \ll b$.

7.6.2 Inputs to the optimization

In order to train the RGS, signal and background samples were prepared from events passing the event selection outlined in Table 7.1 up through the b -jet veto. The signal sample was chosen to be the longitudinally polarized $W^\pm W^\pm jj$ EWK events, and the transverse and mixed polarizations were treated as background along with $W^\pm W^\pm jj$ events from QCD interactions and the traditional backgrounds listed in Section 7.4. Splitting the inclusive $W^\pm W^\pm jj$ EWK events by polarization allows the optimization to favor the longitudinally polarized events as much as possible, even though they both contribute to the EWK signal.

The following variables were chosen for optimization:

- Leading lepton p_T

- 309 • Dilepton invariant mass (m_{ll})
- 310 • Leading and subleading jet p_T
- 311 • Dijet invariant mass (m_{jj})
- 312 • Lepton-jet centrality (ζ)

313 Subleading lepton p_T was omitted as it is desirable to keep the cut value as low as possible due to
 314 its sensitivity to the longitudinal polarization (as discussed in Section 7.3.1). Additionally, the dijet
 315 separation $\Delta\eta_{jj}$ was included in the optimization originally, however it was dropped from the list due
 316 to the cut value being motivated by differences between EWK and QCD produced $W^\pm W^\pm jj$ events.

317 Two additional constraints were imposed when selecting the optimal cut point:

- 318 1. At least 1000 signal events must survive in order to prevent the optimization from being too
 319 aggressive and unnecessarily reducing signal statistics.
- 320 2. The dijet invariant mass may only vary within a 50 GeV range of the default value (from
 321 450-550 GeV) due to the cut being physically motivated by the VBS event topology (**TODO:**
 322 **reference where this is discussed in the 13TeV section**).

323 Lastly, the decision was made to use calculate the signal significance without taking into account
 324 the uncertainty of the background using Equation 7.3. This was due to the fact that the statistical
 325 uncertainties of the fake electron and charge-misID backgrounds were quite large, and if Equation 7.1
 326 were used instead, the optimization would cut unreasonably hard against these backgrounds. Since
 327 Monte Carlo statistics is not expected to be a limiting factor when this analysis is performed at the
 328 HL-LHC, it is more realistic to simply ignore these large statistical uncertainties for the purpose of
 329 the selection optimization.

330 7.6.3 Results of the optimization

331 Ultimately, the random grid was constructed from over 38,000 LL-polarized $W^\pm W^\pm jj$ events in
 332 the variables listed above. After applying the constraints, an optimal cut point was chosen which
 333 reduced the total background from 9900 to 2310 while reducing the signal from 3489 to 2958. This
 334 corresponds to an increase in signal significance from $Z = 33.26$ to $Z = 52.63$ as calculated by
 335 Equation 7.3. The updates to the event selection are listed in Table 7.2.

336 The large reduction in the background is primarily a result of the increase in the leading and
 337 subleading jet p_T from 30 GeV to 90 GeV and 45 GeV, respectively. As can be seen in Figure 7.7,

338 this increase removes a significant portion of the backgrounds from jets faking electrons and charge
 339 mis-ID. Additionally, the loosening of the lepton-jet centrality cut ζ allows more signal events to
 340 survive the event selection (see Figure 7.9). Other changes to the event selection are minor and do
 341 not individually have a large impact on the signal or background yields.

342 The full event yields after optimization as well as the cross section measurement are detailed
 343 alongside those using the default selection in Section 7.7.

344 **TODO: It's a bit awkward to reference the results of the default/optimized before they're prop-**
 345 **erly presented. Maybe move the sections around? not sure...**

Selection requirement	Selection value
Lepton kinematics	$p_T > 28$ GeV (leading lepton only)
Jet kinematics	$p_T > 90$ GeV (leading jet) $p_T > 45$ GeV (subleading jet)
Dilepton mass	$m_{ll} > 28$ GeV
Dijet mass	$m_{jj} > 520$ GeV
Lepton-jet centrality	$\zeta > -0.5$

Table 7.2: Updates to the $W^\pm W^\pm jj$ event selection criteria after optimization. Cuts not listed remain unchanged from the default selection in Table 7.1.

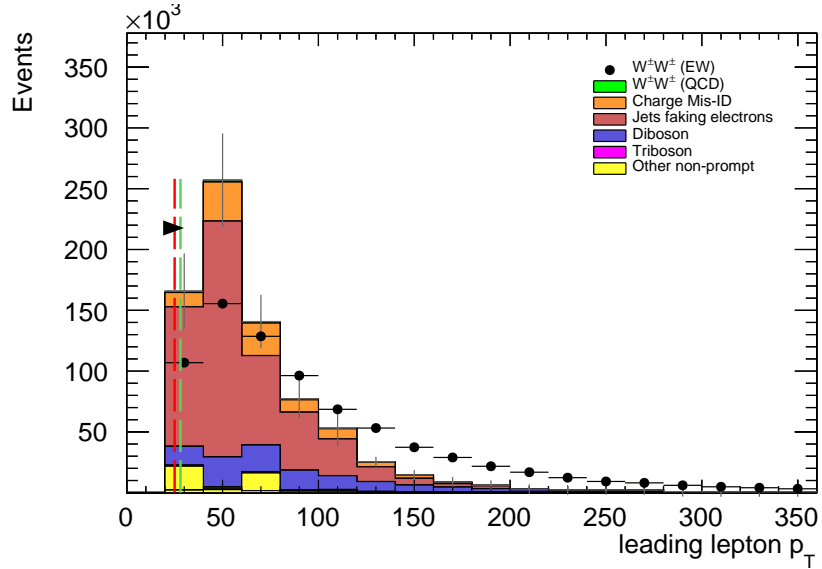


Figure 7.5: Leading lepton p_T distribution. The default and optimized cuts are represented by the red and green dashed lines, respectively. The $W^\pm W^\pm jj$ EWK signal (black points) is normalized to the same area as the sum of the backgrounds (colored histogram). **TODO: Move to appendix or omit**

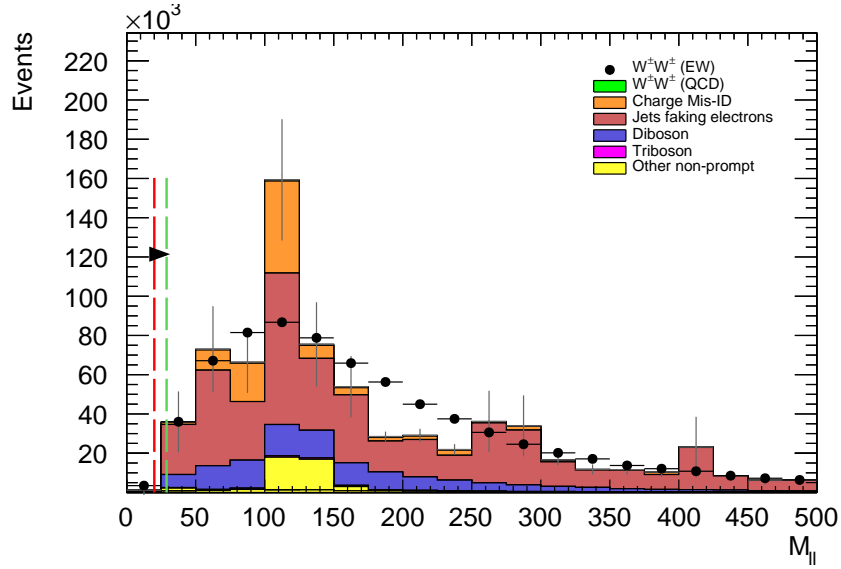


Figure 7.6: Dilepton invariant mass distribution. The default and optimized cuts are represented by the red and green dashed lines, respectively. The $W^\pm W^\pm jj$ EWK signal (black points) is normalized to the same area as the sum of the backgrounds (colored histogram).
 TODO: Move to appendix or omit

346 7.7 Results

347 7.7.1 Event yields

348 7.7.2 Uncertainties

349 7.7.3 Cross section measurement

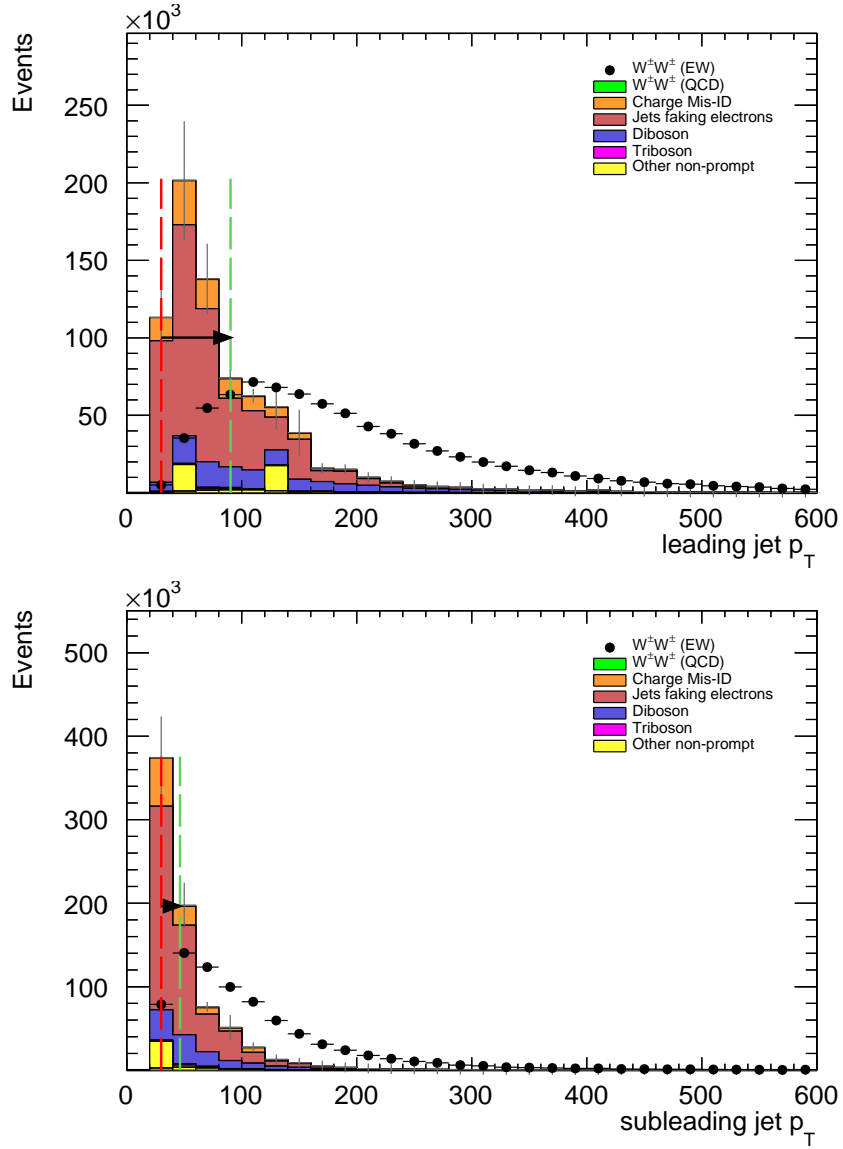


Figure 7.7: Leading (top) and subleading (bottom) jet p_T distributions. The default and optimized cuts are represented by the red and green dashed lines, respectively. The $W^\pm W^\pm jj$ EWK signal (black points) is normalized to the same area as the sum of the backgrounds (colored histogram).

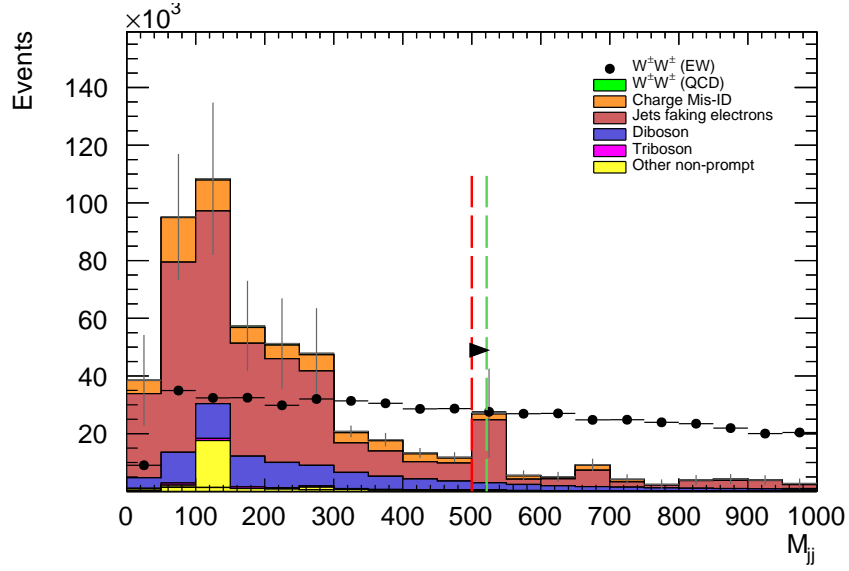


Figure 7.8: Dijet invariant mass distribution. The default and optimized cuts are represented by the red and green dashed lines, respectively. The $W^\pm W^\pm jj$ EWK signal (black points) is normalized to the same area as the sum of the backgrounds (colored histogram). **TODO:** Move to appendix or omit

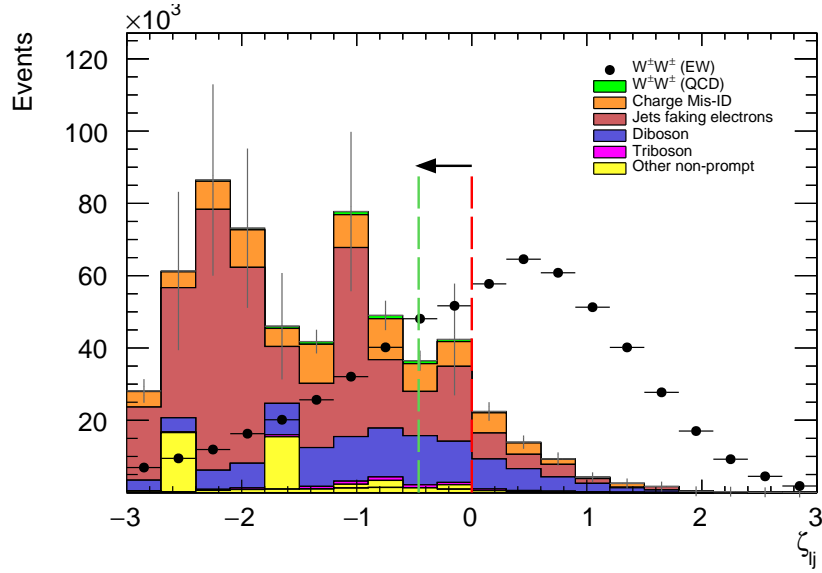


Figure 7.9: Lepton-jet centrality distribution. The default and optimized cuts are represented by the red and green dashed lines, respectively. The $W^\pm W^\pm jj$ EWK signal (black points) is normalized to the same area as the sum of the backgrounds (colored histogram).

350

CHAPTER 8

351

Conclusion

352 Here’s where you wrap it up.

353 **Looking Ahead**

354

355 Here’s an example of how to have an “informal subsection”.

Bibliography

- [1] K. J. Potamianos, W. K. Di Clemente, M.-A. Pleier, C. A. Lee, J. I. Kroll, S. Yacoob, and M. Leigh, *Prospects for the measurement of the $W^\pm W^\pm$ scattering cross section and extraction of the longitudinal scattering component in pp collisions at the High-Luminosity LHC with the ATLAS experiment.*, Tech. Rep. ATL-COM-PHYS-2018-1479, CERN, Geneva, Oct, 2018. <https://cds.cern.ch/record/2644264>. (document), 7.1, 7.2
- [2] S. L. Glashow, *The Renormalizability of Vector Meson Interactions*, *Nucl. Phys.* **10** (1959) 107–117. 2.2
- [3] A. Salam and J. C. Ward, *Weak and Electromagnetic Interactions*, *Nuovo Cimento* **11** (1959) 568–577. 2.2
- [4] L. R. Evans and P. Bryant, *LHC Machine*, *JINST* **3** (2008) S08001. <https://cds.cern.ch/record/1129806>. This report is an abridged version of the LHC Design Report (CERN-2004-003). 3.1
- [5] ATLAS Collaboration, *The ATLAS Experiment at the CERN Large Hadron Collider*, *JINST* **3** (2008) S08003. 3.1
- [6] ATLAS Collaboration Collaboration, *Alignment of the ATLAS Inner Detector Tracking System with 2010 LHC proton-proton collisions at $\sqrt{s} = 7$ TeV*, Tech. Rep. ATLAS-CONF-2011-012, CERN, Geneva, Mar, 2011. <https://cds.cern.ch/record/1334582>. 4
- [7] R. Steerenberg, *LHC Report: Another run is over and LS2 has just begun...*, <https://home.cern/news/news/accelerators/lhc-report-another-run-over-and-ls2-has-just-begun>, 2018. Accessed: 2018-12-14. 7
- [8] *Letter of Intent for the Phase-I Upgrade of the ATLAS Experiment*, Tech. Rep. CERN-LHCC-2011-012. LHCC-I-020, CERN, Geneva, Nov, 2011. <http://cds.cern.ch/record/1402470>. 7
- [9] G. Apollinari, I. Bjar Alonso, O. Brning, M. Lamont, and L. Rossi, *High-Luminosity Large Hadron Collider (HL-LHC): Preliminary Design Report*. CERN Yellow Reports: Monographs. CERN, Geneva, 2015. <https://cds.cern.ch/record/2116337>. 7

- [10] ATLAS Collaboration Collaboration, ATLAS Collaboration, *ATLAS Phase-II Upgrade Scoping Document*, Cern-lhcc-2015-020, Geneva, Sep, 2015.
<http://cds.cern.ch/record/2055248>. 7
- [11] J. Alwall, R. Frederix, S. Frixione, V. Hirschi, F. Maltoni, O. Mattelaer, H. S. Shao, T. Stelzer, P. Torrielli, and M. Zaro, *The automated computation of tree-level and next-to-leading order differential cross sections, and their matching to parton shower simulations*, *JHEP* **07** (2014) 079, [arXiv:1405.0301 \[hep-ph\]](#). 7.2
- [12] R. D. Ball et al., *Parton distributions for the LHC Run II*, *JHEP* **04** (2015) 040, [arXiv:1410.8849 \[hep-ph\]](#). 7.2
- [13] T. Sjöstrand, S. Ask, J. R. Christiansen, R. Corke, N. Desai, P. Ilten, S. Mrenna, S. Prestel, C. O. Rasmussen, and P. Z. Skands, *An Introduction to PYTHIA 8.2*, *Comput. Phys. Commun.* **191** (2015) 159–177, [arXiv:1410.3012 \[hep-ph\]](#). 7.2
- [14] T. Gleisberg et al., *Event generation with SHERPA 1.1*, *JHEP* **02** (2009) 007, [arXiv:0811.4622 \[hep-ph\]](#). 7.2
- [15] S. Schumann and F. Krauss, *A parton shower algorithm based on Catani-Seymour dipole factorization*, *JHEP* **03** (2008) 038, [arXiv:0709.1027 \[hep-ph\]](#). 7.2
- [16] S. Höche, F. Krauss, S. Schumann, and F. Siegert, *QCD matrix elements and truncated showers*, *JHEP* **05** (2009) 053, [arXiv:0903.1219 \[hep-ph\]](#). 7.2
- [17] S. Alioli, P. Nason, C. Oleari, and E. Re, *A general framework for implementing NLO calculations in shower Monte Carlo programs: the POWHEG BOX*, *JHEP* **06** (2010) 043, [arXiv:1002.2581 \[hep-ph\]](#). 7.2
- [18] H.-L. Lai, M. Guzzi, J. Huston, Z. Li, P. M. Nadolsky, J. Pumplin, and C. P. Yuan, *New parton distributions for collider physics*, *Phys. Rev. D* **82** (2010) 074024, [arXiv:1007.2241 \[hep-ph\]](#). 7.2
- [19] S. Agostinelli et al., *GEANT4 - a simulation toolkit*, *Nucl. Instrum. Meth. A* **506** (2003) 250–303. 7.2
- [20] P. C. Bhat, H. B. Prosper, S. Sekmen, and C. Stewart, *Optimizing Event Selection with the Random Grid Search*, *Comput. Phys. Commun.* **228** (2018) 245–257, [arXiv:1706.09907 \[hep-ph\]](#). 7.6.1
- [21] G. Cowan, K. Cranmer, E. Gross, and O. Vitells, *Asymptotic formulae for likelihood-based tests of new physics*, *Eur. Phys. J. C* **71** (2011) 1554, [arXiv:1007.1727 \[physics.data-an\]](#). [Erratum: *Eur. Phys. J. C* **73**, 2501 (2013)]. 7.6.1